

# LineGraph2Road: Structural Graph Reasoning on Line Graphs for Road Network Extraction

Zhengyang Wei<sup>1</sup>, Renzhi Jing<sup>1</sup>, Yiyi He<sup>2</sup>, and Jenny Suckale<sup>1</sup>

<sup>1</sup> Stanford University, Stanford CA 94305, USA

{zywei,rjing,jsuckale}@stanford.edu

<sup>2</sup> Georgia Institute of Technology, Atlanta GA 30332, USA

yiyi.he@design.gatech.edu

**Abstract.** The accurate and automatic extraction of roads from satellite imagery is critical for applications in navigation and urban planning, significantly reducing the need for manual annotation. Many existing methods decompose this task into keypoint extraction and connectedness prediction, but often struggle to capture long-range dependencies and complex topologies. Here, we propose LineGraph2Road, a framework that improves connectedness prediction by formulating it as binary classification over edges in a constructed global but sparse Euclidean graph, where nodes are keypoints extracted from segmentation masks and edges connect node pairs within a predefined distance threshold, representing potential road segments. To better learn structural link representation, we transform the original graph into its corresponding line graph and apply a Graph Transformer on it for connectedness prediction. This formulation overcomes the limitations of endpoint-embedding fusion on set-isomorphic links, enabling rich link representations and effective relational reasoning over the global structure. Additionally, we introduce an overpass/underpass head to resolve multi-level crossings and a coupled NMS strategy to preserve critical connections. We evaluate LineGraph2Road on three benchmarks — City-scale, SpaceNet, and Global-scale and show that it achieves state-of-the-art results on two key metrics, TOPO-F1 and APLS. It also captures fine visual details critical for real-world deployment. We will make our code publicly available.

**Keywords:** Road Network Extraction · Line Graph Transformation · Satellite Imagery

## 1 Introduction

Accurate and up-to-date road maps are essential for a wide range of applications, including navigation systems [26], urban planning [7], and emergency response routing [28]. For example, a city relies on precise maps to dispatch emergency vehicles efficiently [28]. However, many parts of the world lack reliable digital road maps or depend on outdated versions [3], highlighting the urgent need for scalable and automated mapping solutions [8]. High-resolution satellite imagery reduces the manual effort required for large-scale mapping [15], but generating

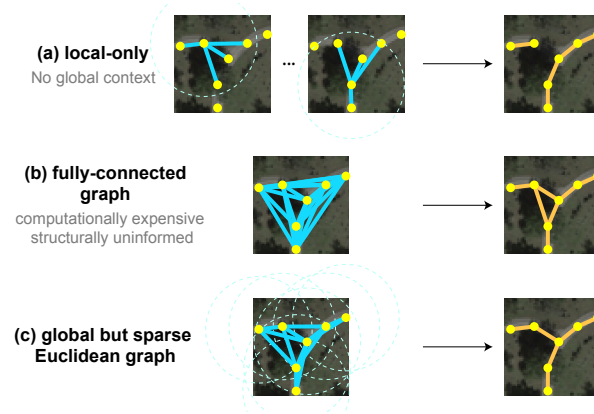


**Fig. 1:** Comparison of graph connectivity strategies. (a) Local-only (*e.g.*, SAM-Road [18]) limits message passing to small subgraphs. (b) Fully-connected (*e.g.*, Any2Graph [24], RelationFormer [31]) enables global reasoning but is computationally costly and structurally uninformed. (c) global but sparse Euclidean graph connects nearby nodes within a distance threshold, balancing global context, structural awareness, and efficiency.

high-quality maps requires broad coverage, accurate road connectivity, and precise mapping of junctions and intersections [17], as even minor errors can lead to major routing failures.

Despite numerous proposed approaches [4, 15, 17, 18, 32, 41, 42, 44, 49], extracting road networks from satellite imagery remains a challenging task for computer vision due to the inherent complexity and diversity of road network structures [15, 17]. To avoid the error-prone post-processing heuristics of purely segmentation-based methods and the parallelization challenges inherent in iterative methods, He *et al.* [17] divide the problem into two subtasks: keypoint prediction and connectedness prediction. We adopt this division for our framework.

For keypoint prediction, we employ the Segment Anything Model (SAM) [23], a foundation model trained on millions of images and billions of masks, recently adapted for road extraction with strong performance [18, 44]. Unlike prior SAM-based methods [18, 44], our framework introduces a dedicated head to explicitly segment overpass and underpass crossings. These crossings represent vertically stacked intersections where roads overlap in image space but remain topologically disconnected in 3D. Accurately modeling such non-planar structures is essential for reconstructing realistic and navigable road networks.

A key design choice in our framework is to reframe the task as edge prediction in a global but sparse Euclidean graph to enable long-range relational reasoning. In contrast, existing methods either restrict reasoning to local neighborhoods [17, 18, 44] or apply dense pairwise attention across all nodes [24, 31, 43], as illustrated in Figure 1. Local-only approaches such as SAM-Road [18] pre-

dict connections within small subgraphs centered on each vertex, overlooking long-range dependencies and limiting global topological understanding [1]. Fully-connected method like Any2Graph [24] and RelationFormer [31] apply dense pairwise attention across all nodes, which is both computationally expensive, structurally uninformed, and prone to error. Our formulation instead connects node pairs within a distance threshold to form a global graph that balances global context and local structure, allowing the model to move beyond local heuristics, reduce computation, and infer connectivity in occluded or ambiguous regions.

To leverage global context for connectedness prediction, we transform the original global but sparse Euclidean graph into its line graph. Prior methods typically use graph autoencoders (GAEs) [36], which aggregate node embeddings to infer links [1]. However, GAEs often fail to capture structural distinctions among links, since edges connecting different node pairs can yield similar aggregated embeddings [47]. We reformulate link prediction as node classification on the line graph [6, 13, 25], where each node corresponds to an edge in the original graph, and adjacency is defined by shared endpoints. This design allows the Graph Transformer to reason directly over link-level features, avoiding indistinguishable endpoint aggregation and producing more expressive structural representations.

To integrate relation reasoning, we first construct a global but sparse Euclidean graph whose vertices are extracted from the keypoint, road, and overpass/underpass segmentation masks using Coupled Non-Maximum Suppression (NMS) [19], with edges formed by connecting all vertex pairs within a predefined distance threshold. We then convert the graph into its line graph, reformulating link prediction as node classification, where each node represents a candidate edge and inherits features from the SAM encoder. A Graph Transformer [30] is applied to the line graph [13] to capture long-range dependencies and learn expressive link representations, forming the core of our connectedness prediction framework. Our contributions can be summarized as follows:

- We propose a new framework, **LineGraph2Road**, which formulates connectedness prediction as binary classification over edges in a global but sparse Euclidean graph where only node pairs within predefined distance are considered rather than fully dense attention or local-only.
- Under a fully unobserved graph setting, a novel strategy of applying Graph Transformer [30] on the line graph transformation of the original graph is proposed to capture expressive structural link representations, avoiding direct endpoint-embedding fusion that fails to distinguish set-isomorphic links.
- Within the framework, we introduce an overpass/underpass segmentation head that explicitly differentiates multi-level crossings and a coupled NMS strategy that preserves critical connections around complex intersections.
- Our method outperforms state-of-the-art methods in topology similarity metrics, TOPO-F1 and APLS, evaluated on three datasets: City-scale [15], SpaceNet [34], and Global-scale [44]. In addition to quantitative improve-

ments, our model excels in visual details that are crucial for real-world applications but are not fully captured by existing metrics.

## 2 Related Work

### 2.1 Road Extraction from Satellite Images

The methods for extracting road network graphs from high-resolution satellite images can be divided into two broad categories: segmentation-based and graph-based methods [15].

**Segmentation-based methods** aim to predict road masks using segmentation models, with various enhancements such as stronger backbones [2, 49], joint orientation learning [5], and improved loss functions [27, 29]. Some of these methods extract the road graph from the segmentation with post-processing heuristics, such as a thinning algorithm [9], A-star path-finding [27] or smoothing-based optimization algorithms [10]. Because post-processing heuristics rely exclusively on predicted segmentation masks without incorporating image-level context, any noise or inaccuracies in the segmentation are inherently propagated to the extracted graph, limiting the accuracy of the topological connectivity inference [4].

**Graph-based methods** output the vectorized road network graph directly. RoadTracer [4] pioneered an iterative search process guided by a CNN-based decision function, followed by improvements from VecRoad [32], RNGDet [41], and RNGDet++ [42], which introduced flexible step sizes, transformers with imitation learning, and instance segmentation heads, respectively. However, such vertex-by-vertex approaches are slow and hard to parallelize because of sequential dependencies, and errors can accumulate over time.

In contrast, holistic methods generate the entire graph in a single forward pass [15, 17, 18, 44]. Sat2Graph [15] encodes the graph as a tensor that captures keypoints and orientations. TD-Road [17] employs two branches for keypoint prediction and relation reasoning. SAM-Road [18] builds on this with the Segment Anything encoder [23] and a transformer-based reasoning module, while SAM-Road++ [44] enhances performance with node-guided resampling and extended-line strategies. kLCRNet [45] uses a similar local connectivity module to directly construct connections between bipartite-matched keypoints using line pooling. However, the relational reasoning in these methods is restricted to each vertex and its immediate neighbors, overlooking potentially long-range dependencies beyond the predefined neighborhood.

### 2.2 Graph Representation Learning

Graph Neural Networks (GNNs) [22, 35, 38] are widely used for road network related tasks, such as road attribute prediction [11, 16, 20] and road representation learning [39, 48]. Gharaee et al. [11] employ a line-graph transformation for road type classification on a known road network, explicitly modeling edge-edge interactions and motivated by the limited features available to describe crossroads

and intersections. For road network graph extraction, SPIN Road Mapper [2] performs graph reasoning on spatial and interaction spaces in the segmentation branch for a better segmentation mask but does not apply directly to the construction of the road network graph. Bahl *et al.* [1] use a GNN [36] to predict links between the detected points of interest, but their approach did not outperform other methods. SAM-Road [23] designs its transformer as a form of Graph Convolutional Networks [22] as a topology decoder, but it only predicts in local subgraphs around individual vertices, overlooking the global topological structure and long-range dependency of the road network.

Image-to-graph methods like RelationFormer [31] and Any2Graph [24] tackle tasks such as network extraction [33] using transformer-based models which use full pairwise attention over all nodes, which is structurally uninformed. These methods typically operate on small, overlapping crops (*e.g.*,  $128 \times 128$  patches), limiting their ability to capture global context. Node identity issues arise because they lack mechanisms to maintain consistent node identifiers across patch boundaries. Reconstruction complexity further emerges as merging patch-level predictions into a single global graph requires non-trivial alignment and deduplication, often introducing additional errors and inconsistencies.

### 3 Method

#### 3.1 Overall Architecture

Figure 2 gives an overview of our LineGraph2Road pipeline. It consists of a pre-trained SAM [23] image encoder and decoder for mask prediction (Section 3.2), a coupled NMS module for vertex extraction (Section 3.3), and a Graph Transformer-based module for connectedness prediction on the line graph (Section 3.4). Given an RGB satellite image as input, the SAM encoder generates feature maps and the decoder predicts probability maps for keypoints, roads, overpass/underpass crossings. Vertices are extracted from the probability maps by using coupled NMS. We treat vertex pairs within a distance threshold as candidate edges, with their features bilinearly sampled from the image feature map. These extracted vertices and candidate edges form a global but sparse Euclidean graph, which is then converted into its line graph. Finally, the line graph is processed by the Graph Transformer to predict binary labels for connectedness.

#### 3.2 Segment Anything Encoder and Decoder for Mask Prediction

We use a pre-trained SAM [23], the ViT-B variant, as our image encoder. The encoder produces a feature map,  $F \in \mathbb{R}^{\frac{H}{16} \times \frac{W}{16} \times D_{\text{feature}}}$ , that is downsampled by a factor of 16 relative to the input image resolution  $H \times W \times 3$ . Following the original SAM design, we use the lightweight mask decoder without any input prompts. The decoder is configured for three output tasks, producing probability maps for the keypoint mask  $\hat{M}_{\text{keypoint}}$ , the road mask  $\hat{M}_{\text{road}}$  and overpass/underpass mask  $\hat{M}_{\text{overpass}}$ .

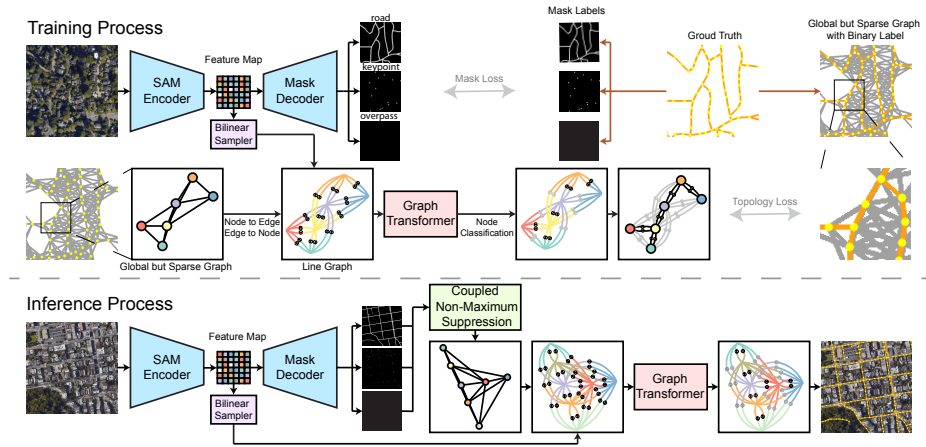


**Fig. 2:** Overview of our LineGraph2Road pipeline. During both training and inference, a satellite image is processed by the pre-trained SAM encoder [23] to extract feature maps, which are decoded into road masks. In training, the graph is constructed from a preprocessed candidate edge set (brown lines), while in inference, it is built from vertices extracted via Coupled NMS on the road mask. This graph is converted into a line graph and passed to a Graph Transformer for binary node classification, determining the presence of links and yielding the final road network graph.

### 3.3 Coupled Non-Maximum Suppression for Vertex Extraction

Based on the keypoint, road and overpass/underpass masks, we adopt the idea of NMS [19] to obtain a set of sparse vertices which should be the node of the final road network graph. We introduce a Coupled NMS algorithm instead of following the strategy [18]. In [18], vertices from two masks are separately extracted, and merged with priority given to intersection vertices, and suppressed by NMS again. In our Coupled NMS algorithm, vertices are first extracted from the keypoint and overpass/underpass mask using a keypoint suppression radius,  $d_k$ , and nearby points in the road mask are suppressed before extracting additional vertices from the road mask using a road suppression radius,  $d_r$ . The full procedure is detailed in Algorithm 1 (Appendix A). Our method not only reduces the failure cases described therein but also achieves a quantitative improvement in overall performance, as reported in Table 4 (Appendix A).

### 3.4 Graph Transformer on Line Graph for Connectedness Prediction

Coupled NMS yields a set of sparse vertices that are likely to be on the road network, but without connectedness information. To construct a graph that provides the model with broader contextual awareness of the road system, we treat vertex pairs within a distance threshold  $d_{nei}$  as candidate edges. We label directly connected pairs as positive examples and others, including routable but indirect

connections, as negative, creating a binary edge classification problem. The set of sparse vertices and the candidate edges can form a global but sparse Euclidean graph,  $G = (V, E_{\text{nei}})$ , where  $E_{\text{nei}} = \{(i, j) \mid i, j \in V, \|\text{pos}(i) - \text{pos}(j)\|_2 \leq d_{\text{nei}}\}$ .

We obtain the feature for each candidate edge by sampling features from the feature map,  $F$ , using bilinear sampling at the two endpoints and a set of uniformly interpolated points. In total, we extract and concatenate  $N_{\text{sampled}}$  features from the first endpoint to the second. This concatenated feature vector is then passed through a multilayer perceptron (MLP) to generate the candidate edge feature.

Beyond using visual features for each candidate edge, we also take into account how the edge fits into the overall structure of the graph. Rather than predicting edge presence by directly aggregating node representations [46] of two endpoints of the edge, we first convert the original graph into a line graph [13],  $L(G)$ .

**Definition 1. (*Line Graph*)** *The line graph  $L(G)$  of a graph  $G$  is a graph where each node in  $L(G)$  corresponds to an edge in  $G$  and two nodes in  $L(G)$  are adjacent if and only if their corresponding edges in  $G$  share a common vertex.*

By converting the graph into its line graph, we reformulate the task as node classification, where each node in  $L(G)$  represents a candidate edge of the original graph with its corresponding features. While prior work has explored line graphs for link prediction [6, 25], our works further demonstrate their effectiveness in learning expressive structural link representations (see Appendix D).

We employ a 3-layer Graph Transformer architecture [30] to maintain a transformer-based design consistent with [18, 44], ensuring that any performance gains arise from graph reasoning rather than differences in model class. For reference, we also compare our model against standard GNN baselines in Appendix D. Let  $\mathbf{X}^{(l)} = \{\mathbf{x}_1^{(l)}, \mathbf{x}_2^{(l)}, \dots, \mathbf{x}_n^{(l)}\}$  denote the node features of the  $l$ -th layer and  $\mathbf{X}^{(0)}$  be the candidate edge feature generated from the image feature map. For each edge from node  $j$  to node  $i$  in  $L(G)$ , we compute the multi-head attention as :

$$\alpha_{c,ij}^{(l)} = \text{softmax} \left( \frac{(\mathbf{W}_{c,q}^{(l)} \mathbf{x}_i^{(l)})^\top (\mathbf{W}_{c,k}^{(l)} \mathbf{x}_j^{(l)})}{\sqrt{d}} \right), \quad (1)$$

where  $c$  indexes the attention head,  $d$  is the hidden dimension per head, and  $\mathbf{W}_{c,q}^{(l)}$  and  $\mathbf{W}_{c,k}^{(l)}$  are trainable parameters. After getting the multi-head attention, we compute the message aggregation for each node  $i$  as:

$$\mathbf{h}_i^{(l)} = \parallel_{c=1}^C \sum_{j \in \mathcal{N}(i)} \alpha_{c,ij}^{(l)} (\mathbf{W}_{c,v}^{(l)} \mathbf{x}_j^{(l)}), \quad (2)$$

where the  $\parallel$  denotes concatenation over all  $C$  attention heads, and  $\mathbf{W}_{c,v}^{(l)}$  is trainable parameters. The aggregated features  $\mathbf{H}^{(l)} = \{\mathbf{h}_1^{(l)}, \mathbf{h}_2^{(l)}, \dots, \mathbf{h}_n^{(l)}\}$  are passed through a residual connection and feedforward layer with layer normalization:

$$\begin{aligned}\mathbf{H}^{(l+1)} &= \text{LN}\left(\mathbf{X}^{(l)} + \text{DO}\left(\mathbf{H}^{(l)}\right)\right), \\ \mathbf{X}^{(l+1)} &= \text{LN}\left(\mathbf{H}^{(l+1)} + \text{DO}\left(W_2^{(l)} \text{ReLU}\left(W_1^{(l)} \mathbf{H}^{(l+1)}\right)\right)\right)\end{aligned}\quad (3)$$

where LN denotes Layer Normalization and DO denotes Dropout.  $W_1^{(l)}$  and  $W_2^{(l)}$  are trainable parameters. Finally, we pass the output node features from the last layer,  $\mathbf{X}^{(3)}$ , through a linear layer followed by a sigmoid activation to produce the binary classification output  $\hat{B}$  for each candidate edge.

### 3.5 Training Process

The training data used as model inputs or targets include: RGB satellite images, road masks, keypoint masks, overpass/underpass mask, and candidate edge pairs with their corresponding endpoint positions and binary labels that indicate whether two endpoints are directly connected.

To construct the road mask,  $M_{\text{road}}$ , we rasterize ground-truth road centerlines into a binary map following [18]. The keypoint mask,  $M_{\text{keypoint}}$ , is obtained by marking all vertices with degree  $\neq 2$ , as well as degree-2 vertices whose adjacent edges form angles between  $60^\circ$  and  $120^\circ$ , rendered as circular regions with a radius of 3 pixels. For the overpass/underpass mask,  $M_{\text{overpass}}$ , we apply Algorithm 3 (Appendix E) to detect endpoints of edges involved in overpass/underpass crossings, which are similarly rendered as circular regions with a radius of 3 pixels.

We then derive candidate edge pairs from the vectorized road network graph. To align with the Coupled NMS vertex set, we include all graph keypoints and interpolate additional points along paths between them at random intervals in  $[d_r, 2d_r]$ , where  $d_r$  is the NMS suppression radius (Algorithm 4 in Appendix E). After applying Coupled NMS and adjusting the endpoints of overpass/underpass edges (Algorithm 3 in Appendix E), candidate edges are formed by connecting vertex pairs within a distance threshold  $d_{\text{nei}}$ , with binary labels  $B$  indicating whether the endpoints are directly connected in the ground-truth graph. The full preprocessing pipeline is illustrated in Figure 10 in Appendix E.

The model is trained end-to-end using RGB images and candidate edge positions as input, and the segmentation masks and binary connectedness labels as supervision. For computational efficiency, images, masks, and graph structures are randomly cropped into smaller patches during training. Our loss function combines the binary cross-entropy (BCE) loss for both mask prediction and connectedness prediction:

$$\mathcal{L} = \mathcal{L}_{BCE}(\hat{M}, M) + \lambda \cdot \mathcal{L}_{BCE}(\hat{B}, B) \quad (4)$$

where  $M = (M_{\text{keypoint}}, M_{\text{road}}, M_{\text{overpass}})$  and  $\hat{M} = (\hat{M}_{\text{keypoint}}, \hat{M}_{\text{road}}, \hat{M}_{\text{overpass}})$ .

### 3.6 Inference Process

During inference, we pass satellite images through the SAM encoder and decoder to obtain the predicted segmentation masks, including the road mask,

keypoint and overpass/underpass mask as shown in Figure 2. We follow the sliding-window approach and the threshold-selection approach in [18] to tackle arbitrarily large regions. We first apply our coupled NMS to process the masks and extract a set of sparse vertices. We then identify candidate edges within a specified distance threshold,  $d_{\text{nei}}$ , construct a global but sparse Euclidean graph and convert to its line graph, and feed it into the Graph Transformer to predict the probability. Since the sliding-window approach may result in the same edge being predicted multiple times, we average the predicted probabilities to obtain the final confidence.

## 4 Experiments

### 4.1 Datasets

We evaluate our method on three benchmarks: City-scale [15], SpaceNet [34], and Global-scale [44]. City-scale contains 180 satellite images ( $2048 \times 2048$ ) from 20 U.S. cities, with 27 used for testing. SpaceNet includes 2,549 images ( $400 \times 400$ ) across Las Vegas, Paris, Shanghai, and Khartoum, with 382 for testing. Global-scale comprises 3,468 images ( $2048 \times 2048$ ) worldwide, with 624 for testing. All datasets have 1 m spatial resolution and provide ground-truth road graphs in adjacency-list format. We adopt the same train/val/test splits as [44].

### 4.2 Metrics

We mainly look at two metrics, TOPO [14] and APLS [34]. TOPO [14] evaluates the geometric and topological alignment between the ground truth and the proposal graphs. It places seed points along ground-truth graphs, samples subgraphs from seed points, and performs a one-to-one matching of points based on spatial and angular thresholds to compute precision, recall, and F1 scores. APLS [34] measures the difference between the ground truth and proposal graphs with the differences in the shortest path lengths between corresponding nodes in both graphs.

### 4.3 Implementation Details

For the City-scale and Global-scale dataset, we randomly crop  $512 \times 512$  patches from  $2048 \times 2048$  images with a batch size of 4. For the SpaceNet dataset, we use the original  $400 \times 400$  images with the same batch size. During training, we randomly rotate patches by multiples of 90 degrees to enhance robustness. The SAM encoder outputs feature maps with a dimensionality of  $D_{\text{feature}} = 128$ . We set the keypoint suppression radius  $d_k$  to 8 and the road suppression radius  $d_r$  to 16. To construct the graph, vertex pairs within a local neighborhood threshold  $d_{\text{nei}} = 64$  are considered candidate edges. For each candidate edge, we extract  $N_{\text{sampled}} = 4$  positions of features from the feature map using bilinear interpolation along the edge. The number of attention heads for the Graph Transformer

$C$  is set to 4. The dimension of the hidden layer in the Graph Transformer is 128. The dropout rate for the Graph Transformer is 0.1. We use the Adam optimizer [21] with a base learning rate of 0.001 for all parameters, except for the pre-trained SAM encoder, which uses a learning rate scaled to  $0.05\times$  the base rate. The  $\lambda$  in the loss function is set to 0.1. For the SpaceNet and City-scale datasets, we train LineGraph2Road for 10 epochs, consistent with the training process of SAM-Road [18] for fair comparison. For the Global-scale dataset, we train LineGraph2Road for 20 epochs, with a learning rate scheduler applied after 10 epochs using  $\gamma = 0.1$ . During inference, we apply a  $16\times 16$  sliding window for the City-scale and Global-scale datasets, while the SpaceNet dataset is processed without sliding window. All experiments are conducted using four NVIDIA A100 GPUs.

#### 4.4 Comparative Results

**Table 1:** Comparison with existing methods on City-scale and SpaceNet datasets.

Methods	City-scale Dataset				SpaceNet Dataset			
	Prec.↑	Rec.↑	F1↑	APLS↑	Prec.↑	Rec.↑	F1↑	APLS↑
RoadTracer [4]	78.00	57.44	66.16	57.29	78.61	62.45	69.90	56.03
Sat2Graph [15]	80.70	72.28	76.26	63.14	85.93	76.55	80.97	64.43
TD-Road [17]	81.94	71.63	76.43	65.74	84.81	<b>77.80</b>	81.15	65.15
RNGDet [41]	85.97	69.78	76.87	65.75	90.91	73.25	81.13	65.61
RNGDet++ [42]	85.65	72.58	78.44	67.76	91.34	75.24	82.51	67.73
SAM-Road [18]	90.47	67.69	77.23	68.37	93.03	70.97	80.52	71.64
SAM-Road++ [44]	88.39	73.39	80.01	68.34	<b>93.68</b>	72.23	81.57	73.44
kLCRNet [45]	86.77	71.59	78.27	68.96	89.69	72.20	80.00	67.51
<b>Ours</b>	91.09	75.44	82.37	68.88	92.82	77.11	<b>84.24</b>	<b>73.94</b>
<b>Ours w/ Overpass</b>	<b>92.75</b>	<b>76.64</b>	<b>83.77</b>	<b>70.40</b>	93.50	76.38	84.08	73.36

We benchmark LineGraph2Road, with and without the overpass/underpass head, on City-scale and SpaceNet dataset against other methods as shown in Table 1. We compare several baselines, including RoadTracer [4], Sat2Graph [15], TD-Road [17], RNGDet [41], RNGDet++ [42], SAM-Road [18], SAM-Road++ [44] and kLCRNet [45]. On the City-scale dataset, LineGraph2Road with overpass head achieves a new state-of-the-art across all TOPO metrics, precision, recall, F1, and APLS, with a clear improvement in topological accuracy. On the SpaceNet dataset, LineGraph2Road without overpass head achieves the highest F1 and APLS. Although its precision (92.82) is slightly lower than the highest reported by SAM-Road++ (93.68), and its recall (77.11) is marginally below that of TD-Road (77.80), our method achieves the best balance between the two. Unlike previous methods that tend to favor high precision or high recall, LineGraph2Road maintains consistently strong performance on both, leading to

a more complete and accurate road graph extraction than previous approaches. The superior performance of the non-overpass variant on SpaceNet is likely due to the scarcity of overpass structures in this dataset. SpaceNet contains only 387 overpass/underpass structures across 408 km<sup>2</sup> (fewer than 1 per km<sup>2</sup>), compared to the City-scale dataset, which has 4,180 structures over 720 km<sup>2</sup> (about 6 per km<sup>2</sup>).

We also evaluate our model on the recently released Global-scale dataset, using in-domain test sets, as summarized in Table 2. LineGraph2Road achieves the highest scores in recall, F1, and APLS, although its precision is relatively lower. The improvement is most notable on APLS, where LineGraph2Road reaches 68.70, substantially higher than the previous best of 62.19, demonstrating its strong ability to capture road connectivity. The failure cases of Global-scale dataset are further analyzed in the Appendix F.2.

**Table 2:** Comparison with existing methods on Global-Scale (In-Domain) dataset.

Methods	Global-Scale (In-Domain)			
	Prec.↑	Rec.↑	F1↑	APLS↑
Sat2Graph [15]	90.15	22.13	35.53	26.77
RNGDet [41]	79.89	40.72	52.59	49.43
RNGDet++ [42]	79.02	45.23	55.04	52.72
SAM-Road [18]	<b>91.93</b>	45.64	59.80	59.08
SAM-Road++ [44]	88.95	49.27	62.33	62.19
<b>Ours</b>	90.54	<b>51.12</b>	<b>64.43</b>	67.69
<b>Ours w/ Overpass</b>	89.65	50.85	64.05	<b>68.70</b>

Qualitative examples of road networks predicted by LineGraph2Road are shown in Figure 3 and Figure 4. The visualizations are shown alongside four competitive baselines [15, 18, 42, 44] and the corresponding ground truth annotations. In general, LineGraph2Road shows strong performance in challenging conditions, such as small roundabouts at intersections, multilane highways with complex merges and curves, and winding roads with irregular geometries as shown in Figure 3. Figure 4 presents overpass/underpass cases comparing predictions from baseline methods and our non-overpass variant, along with the corresponding overpass/underpass mask. The results illustrate that our model effectively identifies the relevant regions and reliably reconstructs multi-level crossings, whereas other methods fail to distinguish or maintain their connectivity. We provide additional qualitative examples in the Appendix F.1.

#### 4.5 Ablation Studies

We conduct ablation experiments to evaluate the impact of key components in LineGraph2Road on the City-scale dataset. To ensure fair comparison, we use

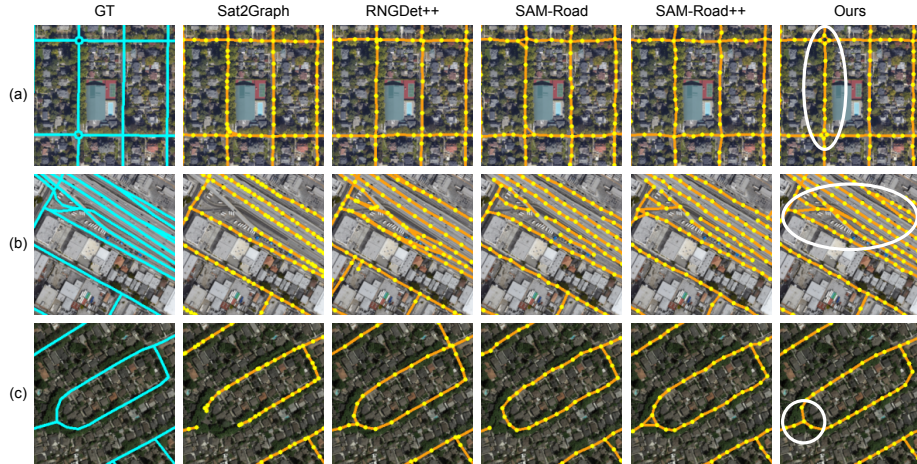


**Fig. 3:** The visualized road network graph predictions of our method and other baseline methods on City-Scale dataset. (a) small roundabouts; (b) multi-lane highways with complex merges and curves; and (c) winding roads with irregular geometries.

**Table 3:** Ablation study on City-scale dataset.

Variant	Setting				City-scale Dataset				
	SAM Image Feature	Line Graph	Graph Transformer		$N_{\text{sampled}}$	Prec.↑	Rec.↑	F1↑	APLS↑
-	✓	✓	✓	✓	4	91.09	75.44	82.37	68.88
A		✓	✓	✓	4	89.29	68.19	77.08	61.63
B	✓		✓	✓	4	80.93	72.20	76.12	69.17
C	✓	✓	✓		4	92.12	65.51	76.12	55.84
D	✓	✓	✓	to 3-layer MLP	4	93.03	62.36	74.20	52.20
E	✓	✓	✓	✓	8	91.29	75.27	82.34	68.91
F	✓	✓	✓	✓	2	91.29	75.11	82.25	68.11
G	✓	✓		✓	2	91.81	73.34	81.35	65.72
H	✓	✓		to RelationFormer decoder [31]	2	92.67	69.07	78.82	60.70
I	✓	✓		to Any2Graph decoder [24]	2	92.98	66.96	77.53	57.38

the non-overpass version to eliminate variability introduced by the overpass head as shown in Appendix C. Results are shown in Table 3.

**Pretrained SAM.** For Variant A, we use the ViT-B encoder without pretrained weights from SAM. Under identical training conditions, the variant with pretrained weights significantly outperforms the one without, demonstrating the effectiveness of pretrained initialization.

**Visual features for guiding connectedness prediction.** For Variant B, we remove the SAM-derived image features and replace them with a learnable pseudo-feature map for candidate edge embedding, allowing us to isolate the contribution of visual features. This control is necessary because bilinear sampling can introduce implicit location cues. Although vertex extraction still relies on SAM during inference, connectivity prediction in this variant depends solely on the pseudo-feature map. This modification leads to a significant drop in precision

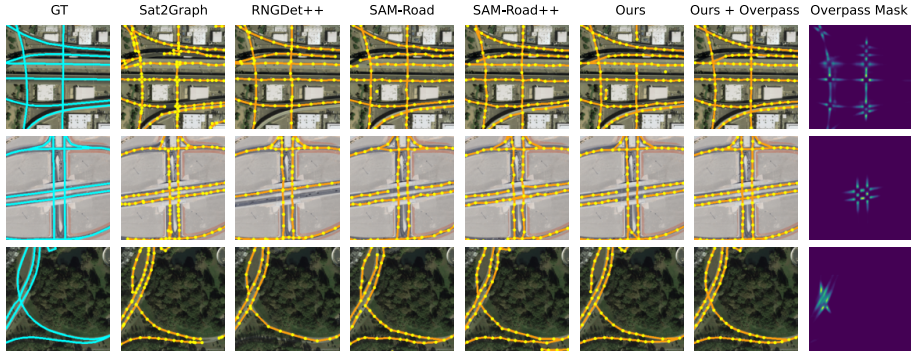


**Fig. 4:** The visualized road network graph predictions of our method and other baseline methods as well as the predicted overpass/underpass mask on City-Scale dataset, illustrating performance on overpass and underpass crossings.

and F1 score, underscoring the importance of visual features in filtering topologically plausible yet visually incorrect connections. The results confirm that location cues alone are insufficient for reliable connectivity prediction. Interestingly, APLS improves slightly, suggesting that this metric may favor topological continuity even when some visually implausible connections are introduced.

**Graph Transformer.** For Variant C, we completely remove the Graph Transformer and instead feed the features extracted from the feature map directly into a fully connected layer for classification. In this setting, link predictions are made independently, without awareness of surrounding connections or graph context. As a result, both TOPO and APLS metrics decline. We further experiment with replacing the Graph Transformer with a 3-layer MLP as variant D. The primary difference lies in the absence of message passing via multi-head attention. This variant performs even worse across both metrics. These results highlight the importance of relational reasoning: relying solely on visual features without considering the patterns of neighboring nodes makes it extremely difficult for the model to accurately infer road connection.

**Number of sampled features per candidate edge.** For Variants E and F, we modify the number of sampled features per candidate edge to 8 and 2, respectively, and compare the results with the default setting of 4. The results show minimal variation in both TOPO and APLS metrics, indicating that intermediate point interpolation provides limited benefit and that additional samples yield diminishing returns.

**Superiority of the line graph transformation over the original graph.** For Variant G, we conducted an ablation comparing the Graph Transformer applied on the original graph versus on the line graph, while keeping all other components, including SAM encoder, mask decoder, coupled NMS, bilinear sampler, identical. We used the sampled feature as node features as the original graph and applied a Graph Transformer with the same architecture on the original

graph, and concatenated the output feature of two endpoints for each edge and passed it to a 3-layer MLP to get the final prediction and compare it with our line graph version. Compared to Variant F with identical features, the original graph variant underperforms significantly, particularly on the APLS metric (65.71 vs 68.11), supporting our analysis in Appendix D that aggregating node representations in a standard GNN constrains the expressiveness of structural link representations.

**Comparison with other link prediction modules.** For Variants H and I, we keep the SAM encoder–decoder fixed and replace only the link prediction modules with those from RelationFormer [31] and Any2Graph [24]. This setup allows us to isolate and verify that the performance improvements originate from our Graph Transformer on the Line Graph, rather than from the powerful SAM backbone. When compared to Variant G, their performance is even worse, likely because the Graph Transformer in Variant G operates on a global but sparse Euclidean graph, whereas RelationFormer and Any2Graph perform on a fully connected graph that lacks structural priors.

## 5 Conclusion

We present LineGraph2Road, an end-to-end framework for extracting road network graphs from satellite images. LineGraph2Road captures long-range dependencies by formulating connectedness prediction as edge classification on a global but sparse Euclidean graph, and learns expressive structural link representations via line graph transformation, enabling more reliable road network predictions than existing methods. In addition, we introduce an overpass/underpass head to handle multi-level crossings and a coupled NMS strategy to preserve critical connections. Our experiments demonstrate that LineGraph2Road achieves better performance on three existing public datasets without introducing significant inference overhead. Our framework advances our ability to automatically detect complete and accurate road maps, including complex non-planar structures such as highway overpasses, which can benefit navigation, disaster response, and urban planning, particularly in regions lacking detailed infrastructure maps or after events that destroyed significant portions of the road infrastructure.

## References

1. Bahl, G., Bahri, M., Lafarge, F.: Single-shot end-to-end road graph extraction. In: Proceedings of the IEEE/CVF Conference on Computer Vision and Pattern Recognition. pp. 1403–1412 (2022)
2. Bandara, W.G.C., Valanarasu, J.M.J., Patel, V.M.: Spin road mapper: Extracting roads from aerial images via spatial and interaction space graph reasoning for autonomous driving. In: 2022 International Conference on Robotics and Automation (ICRA). pp. 343–350. IEEE (2022)
3. Barrington-Leigh, C., Millard-Ball, A.: The world’s user-generated road map is more than 80% complete. PloS one **12**(8), e0180698 (2017)

4. Bastani, F., He, S., Abbar, S., Alizadeh, M., Balakrishnan, H., Chawla, S., Madden, S., DeWitt, D.: Roadtracer: Automatic extraction of road networks from aerial images. In: Proceedings of the IEEE conference on computer vision and pattern recognition. pp. 4720–4728 (2018)
5. Batra, A., Singh, S., Pang, G., Basu, S., Jawahar, C., Paluri, M.: Improved road connectivity by joint learning of orientation and segmentation. In: Proceedings of the IEEE/CVF conference on computer vision and pattern recognition. pp. 10385–10393 (2019)
6. Cai, L., Li, J., Wang, J., Ji, S.: Line graph neural networks for link prediction. *IEEE Trans. Pattern Anal. Mach. Intell.* **44**(9), 5103–5113 (2021)
7. Chen, H., Li, Z., Wu, J., Xiong, W., Du, C.: Semiroadexnet: A semi-supervised network for road extraction from remote sensing imagery via adversarial learning. *ISPRS Journal of Photogrammetry and Remote Sensing* **198**, 169–183 (2023)
8. Chen, H., Qi, Z., Shi, Z.: Remote sensing image change detection with transformers. *IEEE Transactions on Geoscience and Remote Sensing* **60**, 1–14 (2021)
9. Cheng, G., Wang, Y., Xu, S., Wang, H., Xiang, S., Pan, C.: Automatic road detection and centerline extraction via cascaded end-to-end convolutional neural network. *IEEE Transactions on Geoscience and Remote Sensing* **55**(6), 3322–3337 (2017)
10. Costea, D., Marcu, A., Slusanschi, E., Leordeanu, M.: Creating roadmaps in aerial images with generative adversarial networks and smoothing-based optimization. In: Proceedings of the IEEE International Conference on Computer Vision Workshops. pp. 2100–2109 (2017)
11. Gharaee, Z., Kowshik, S., Stromann, O., Felsberg, M.: Graph representation learning for road type classification. *Pattern Recognition* **120**, 108174 (2021)
12. Hamilton, W., Ying, Z., Leskovec, J.: Inductive representation learning on large graphs. *Advances in neural information processing systems* **30** (2017)
13. Harary, F., Norman, R.Z.: Some properties of line digraphs. *Rendiconti del circolo matematico di palermo* **9**, 161–168 (1960)
14. He, S., Bastani, F., Abbar, S., Alizadeh, M., Balakrishnan, H., Chawla, S., Madden, S.: Roadrunner: improving the precision of road network inference from gps trajectories. In: Proceedings of the 26th ACM SIGSPATIAL international conference on advances in geographic information systems. pp. 3–12 (2018)
15. He, S., Bastani, F., Jagwani, S., Alizadeh, M., Balakrishnan, H., Chawla, S., Elshrif, M.M., Madden, S., Sadeghi, M.A.: Sat2graph: Road graph extraction through graph-tensor encoding. In: *Computer Vision–ECCV 2020: 16th European Conference, Glasgow, UK, August 23–28, 2020, Proceedings, Part XXIV* 16. pp. 51–67. Springer (2020)
16. He, S., Bastani, F., Jagwani, S., Park, E., Abbar, S., Alizadeh, M., Balakrishnan, H., Chawla, S., Madden, S., Sadeghi, M.A.: Roadtagger: Robust road attribute inference with graph neural networks. In: Proceedings of the AAAI Conference on Artificial Intelligence. vol. 34, pp. 10965–10972 (2020)
17. He, Y., Garg, R., Chowdhury, A.R.: Td-road: Top-down road network extraction with holistic graph construction. In: *European Conference on Computer Vision*. pp. 562–577. Springer (2022)
18. Hetang, C., Xue, H., Le, C., Yue, T., Wang, W., He, Y.: Segment anything model for road network graph extraction. In: *CVPR Workshop*. pp. 2556–2566 (2024)
19. Hosang, J., Benenson, R., Schiele, B.: Learning non-maximum suppression. In: Proceedings of the IEEE conference on computer vision and pattern recognition. pp. 4507–4515 (2017)

20. Jepsen, T.S., Jensen, C.S., Nielsen, T.D.: Graph convolutional networks for road networks. In: Proceedings of the 27th ACM SIGSPATIAL international conference on advances in geographic information systems. pp. 460–463 (2019)
21. Kingma, D.P.: Adam: A method for stochastic optimization. arXiv preprint arXiv:1412.6980 (2014)
22. Kipf, T.N., Welling, M.: Semi-supervised classification with graph convolutional networks. arXiv preprint arXiv:1609.02907 (2016)
23. Kirillov, A., Mintun, E., Ravi, N., Mao, H., Rolland, C., Gustafson, L., Xiao, T., Whitehead, S., Berg, A.C., Lo, W.Y., et al.: Segment anything. In: Proceedings of the IEEE/CVF international conference on computer vision. pp. 4015–4026 (2023)
24. Krzakala, P., Yang, J., Flamary, R., d’Alché Buc, F., Laclau, C., Labeau, M.: Any2graph: Deep end-to-end supervised graph prediction with an optimal transport loss. *Advances in Neural Information Processing Systems* **37**, 101552–101588 (2024)
25. Lachi, V., Ferrini, F., Longa, A., Lepri, B., Passerini, A.: A simple and expressive graph neural network based method for structural link representation. In: ICML Workshop (2024)
26. Levinson, J., Askeland, J., Becker, J., Dolson, J., Held, D., Kammel, S., Kolter, J.Z., Langer, D., Pink, O., Pratt, V., et al.: Towards fully autonomous driving: Systems and algorithms. In: 2011 IEEE intelligent vehicles symposium (IV). pp. 163–168. IEEE (2011)
27. Mátyus, G., Luo, W., Urtasun, R.: Deeproadmapper: Extracting road topology from aerial images. In: Proceedings of the IEEE international conference on computer vision. pp. 3438–3446 (2017)
28. Mnih, V., Hinton, G.E.: Learning to detect roads in high-resolution aerial images. In: Computer Vision–ECCV 2010: 11th European Conference on Computer Vision, Heraklion, Crete, Greece, September 5–11, 2010, Proceedings, Part VI 11. pp. 210–223. Springer (2010)
29. Mosinska, A., Marquez-Neila, P., Koziński, M., Fua, P.: Beyond the pixel-wise loss for topology-aware delineation. In: Proceedings of the IEEE conference on computer vision and pattern recognition. pp. 3136–3145 (2018)
30. Shi, Y., Zhengjie, H., Feng, S., Zhong, H., Wang, W., Sun, Y.: Masked label prediction: Unified message passing model for semi-supervised classification. In: Proceedings of the Thirtieth International Joint Conference on Artificial Intelligence. pp. 1548–1554 (08 2021). <https://doi.org/10.24963/ijcai.2021/214>
31. Shit, S., Koner, R., Wittmann, B., Paetzold, J., Ezhov, I., Li, H., Pan, J., Sharifzadeh, S., Kaissis, G., Tresp, V., et al.: Relationformer: A unified framework for image-to-graph generation. In: European conference on computer vision. pp. 422–439. Springer (2022)
32. Tan, Y.Q., Gao, S.H., Li, X.Y., Cheng, M.M., Ren, B.: Vecroad: Point-based iterative graph exploration for road graphs extraction. In: Proceedings of the IEEE/CVF Conference on Computer Vision and Pattern Recognition. pp. 8910–8918 (2020)
33. Tetteh, G., Efremov, V., Forkert, N.D., Schneider, M., Kirschke, J., Weber, B., Zimmer, C., Piraud, M., Menze, B.H.: Deepvesselnet: Vessel segmentation, center-line prediction, and bifurcation detection in 3-d angiographic volumes. *Frontiers in Neuroscience* **14**, 592352 (2020)
34. Van Etten, A., Lindenbaum, D., Bacastow, T.M.: Spacenet: A remote sensing dataset and challenge series. arXiv preprint arXiv:1807.01232 (2018)
35. Veličković, P., Cucurull, G., Casanova, A., Romero, A., Lio, P., Bengio, Y.: Graph attention networks. arXiv preprint arXiv:1710.10903 (2017)

36. Wang, Y., Sun, Y., Liu, Z., Sarma, S.E., Bronstein, M.M., Solomon, J.M.: Dynamic graph cnn for learning on point clouds. *ACM Transactions on Graphics (tog)* **38**(5), 1–12 (2019)
37. Whitney, H.: Congruent graphs and the connectivity of graphs. *American Journal of Mathematics* pp. 61–79 (1932)
38. Wu, F., Souza, A., Zhang, T., Fifty, C., Yu, T., Weinberger, K.: Simplifying graph convolutional networks. In: *International conference on machine learning*. pp. 6861–6871. Pmlr (2019)
39. Wu, N., Zhao, X.W., Wang, J., Pan, D.: Learning effective road network representation with hierarchical graph neural networks. In: *Proceedings of the 26th ACM SIGKDD international conference on knowledge discovery & data mining*. pp. 6–14 (2020)
40. Xu, K., Hu, W., Leskovec, J., Jegelka, S.: How powerful are graph neural networks? *arXiv preprint arXiv:1810.00826* (2018)
41. Xu, Z., Liu, Y., Gan, L., Sun, Y., Wu, X., Liu, M., Wang, L.: Rngdet: Road network graph detection by transformer in aerial images. *IEEE Transactions on Geoscience and Remote Sensing* **60**, 1–12 (2022)
42. Xu, Z., Liu, Y., Sun, Y., Liu, M., Wang, L.: Rngdet++: Road network graph detection by transformer with instance segmentation and multi-scale features enhancement. *IEEE Robotics and Automation Letters* **8**(5), 2991–2998 (2023)
43. Yang, B., Zhang, M., Zhang, Z., Zhang, Z., Hu, X.: Topdig: Class-agnostic topological directional graph extraction from remote sensing images. In: *Proceedings of the IEEE/CVF Conference on Computer Vision and Pattern Recognition*. pp. 1265–1274 (2023)
44. Yin, P., Li, K., Cao, X., Yao, J., Liu, L., Bai, X., Zhou, F., Meng, D.: Towards satellite image road graph extraction: A global-scale dataset and a novel method. In: *CVPR* (2025)
45. Zhang, M., Wang, B., Yang, S., Liu, Q., Wang, Y.: klcnet: Fast road network extraction via keypoint-driven local connectivity exploration. *IEEE Journal of Selected Topics in Applied Earth Observations and Remote Sensing* (2025)
46. Zhang, M., Chen, Y.: Link prediction based on graph neural networks. *Advances in neural information processing systems* **31** (2018)
47. Zhang, M., Li, P., Xia, Y., Wang, K., Jin, L.: Labeling trick: A theory of using graph neural networks for multi-node representation learning. *Advances in Neural Information Processing Systems* **34**, 9061–9073 (2021)
48. Zhou, H., Huang, W., Chen, Y., He, T., Cong, G., Ong, Y.S.: Road network representation learning with the third law of geography. *Advances in Neural Information Processing Systems* **37**, 11789–11813 (2024)
49. Zhou, L., Zhang, C., Wu, M.: D-linknet: Linknet with pretrained encoder and dilated convolution for high resolution satellite imagery road extraction. In: *Proceedings of the IEEE conference on computer vision and pattern recognition workshops*. pp. 182–186 (2018)

## A Coupled Non-Maximum Suppression

### A.1 Algorithm

Instead of following the original strategy [18] that separately extracts vertices from both masks, merges them with priority given to intersection vertices, and then applies NMS again, we introduce a Coupled NMS algorithm. In this approach, vertices are first extracted from the keypoint mask using a keypoint suppression radius  $d_k$ , and nearby points in the road mask are suppressed before extracting additional vertices from the road mask using a road suppression radius  $d_r$ .

### A.2 Analysis

The main advantage of the coupled process is to effectively avoid the challenging failure cases encountered in the NMS strategies used in [18, 44] as illustrated in Figure 5.

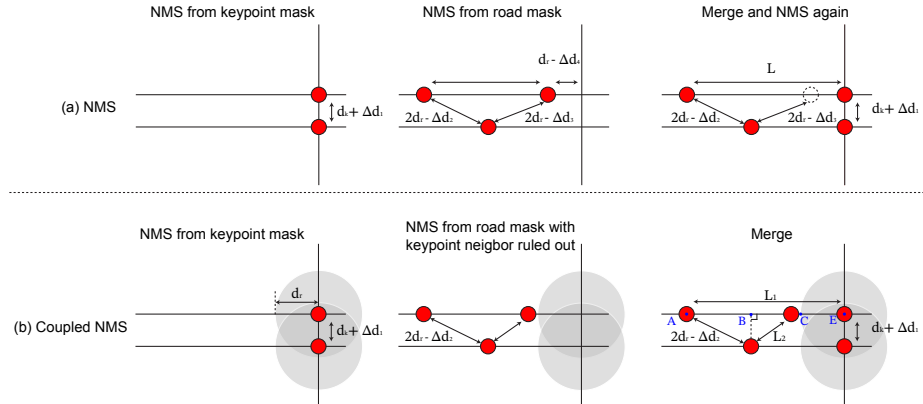


**Fig. 5:** NMS vs Couple NMS. (a) Situation that will happen in NMS strategies used in [18, 44]. (b) How coupled NMS avoid this situation.

In the general setting, we have  $d_r = 2 \cdot d_k$ , and  $d_{nei} = 4 \cdot d_r$ . The described situation is likely to occur when  $\Delta d_1, \Delta d_2, \Delta d_3, \Delta d_4 > 0$ .

$$\begin{aligned}
 L = & \sqrt{(2 \cdot d_r - \Delta d_2)^2 - (d_k + \Delta d_1)^2} \\
 & + \sqrt{(2 \cdot d_r - \Delta d_3)^2 - (d_k + \Delta d_1)^2} \\
 & + (d_r + \Delta d_4)
 \end{aligned} \tag{5}$$

---

**Algorithm 1** Coupled Non-Maximum Suppression of Vertices
 

---

```

1:  $V, V_k, V_o \leftarrow \emptyset$ 
2:  $t_k, t_r \leftarrow$  keypoint and road threshold values
3:  $d_k, d_r \leftarrow$  suppression radius for keypoint and road
4: for each pixel  $(x, y)$  in the keypoint mask do
5:   if pixel value  $> t_k$  then
6:     Add  $(x, y)$  to  $V_o$ 
7:   end if
8: end for
9: Sort  $V_o$  by pixel values in descending order
10: for each  $(x, y)$  in  $V_o$  do
11:   Remove all  $(x', y')$  after  $(x, y)$  in  $V_o$  where  $\text{distance}((x', y'), (x, y)) < d_k$ 
12: end for
13: for each pixel  $(x, y)$  in the overpass/underpass mask do
14:   if pixel value  $> t_k$  then
15:     Add  $(x, y)$  to  $V_k$ 
16:   end if
17: end for
18: Sort  $V_k$  by pixel values in descending order
19: for each  $(x, y)$  in  $V_k$  do
20:   Remove all  $(x', y')$  after  $(x, y)$  in  $V_k$  where  $\text{distance}((x', y'), (x, y)) < d_k$ 
21: end for
22:  $V_k \leftarrow V_k \cup V_o$ 
23: for each pixel  $(x, y)$  in the road mask do
24:   if pixel value  $> t_r$  then
25:     Add  $(x, y)$  to  $V$ 
26:   end if
27: end for
28: for each  $(x_k, y_k)$  in  $V_k$  do
29:   Remove all  $(x, y)$  from  $V$  where  $\text{distance}((x, y), (x_k, y_k)) < d_r$ 
30: end for
31: Sort  $V$  by pixel values in descending order
32: for each  $(x, y)$  in  $V$  do
33:   Remove all  $(x', y')$  after  $(x, y)$  in  $V$  where  $\text{distance}((x', y'), (x, y)) < d_r$ 
34: end for
35:  $V \leftarrow V \cup V_k$ 
36: return  $V$ 

```

---

Assume  $\Delta d_1 = \Delta d_2 = \Delta d_3 = \Delta d_4 = \frac{d_r}{M}$  and we choose  $M = \frac{20}{3}$ , then we have

$$\begin{aligned}
L &= \sqrt{(2 \cdot d_r - \frac{d_r}{M})^2 - (\frac{d_r}{2} + \frac{d_r}{M})^2} \\
&\quad + \sqrt{(2 \cdot d_r - \frac{d_r}{M})^2 - (\frac{d_r}{2} + \frac{d_r}{M})^2} + (d_r + \frac{d_r}{M}) \\
&= 2 \cdot d_r \cdot \sqrt{(2 - \frac{1}{M})^2 - (\frac{1}{2} + \frac{1}{M})^2} + (d_r + \frac{d_r}{M}) \\
&= (2 \cdot \sqrt{\frac{15}{4} - \frac{5}{M}} + 1 + \frac{1}{M}) \cdot d_r > 4 \cdot d_r
\end{aligned}$$

This demonstrates that there exist situations where two vertices should be connected by an edge in the road network graph, yet the distance between them exceeds  $4 \cdot d_r$ .

**Lemma 1.** *The proposed Coupled NMS effectively avoids this situation by ensuring that at least one of the conditions  $L_1 < 4 \cdot d_r$  or  $L_2 > d_r$  is satisfied.*

*Proof.* We first assume the first condition is not satisfied, i.e.  $L_1 \geq 4 \cdot d_r$ , then

$$\begin{aligned}
L_1 \geq 4 \cdot d_r &\iff \overline{BC} = L_1 - \overline{AB} - \overline{CE} > d_r \\
&\quad (\overline{CE} = d_r \text{ and } \overline{BC} < 2 \cdot d_r - \Delta d_2) \\
&\iff L_2 > \overline{BC} > d_r
\end{aligned}$$

which means that if  $L_1 > 4 \cdot d_r$ , then NMS will keep one vertex between  $B$  and  $C$  on the road network graph.

We then assume the second condition is not satisfied, i.e.  $L_2 \leq d_r$ , then

$$\begin{aligned}
L_2 \leq d_r &\iff \overline{BC} < L_2 \leq d_r \\
&\iff L_1 = \overline{AB} + \overline{BC} + \overline{CE} \\
&\quad < 2 \cdot d_r - \Delta d_2 + d_r + d_r \\
&\quad < 4 \cdot d_r
\end{aligned}$$

which means that if we couldn't find any vertex between  $B$  and  $C$  satisfying the NMS threshold condition, then  $L_1 < 4 \cdot d_r$ , won't exceed the pair neighborhood threshold.

### A.3 Comparative Analysis of Coupled vs. Standard NMS

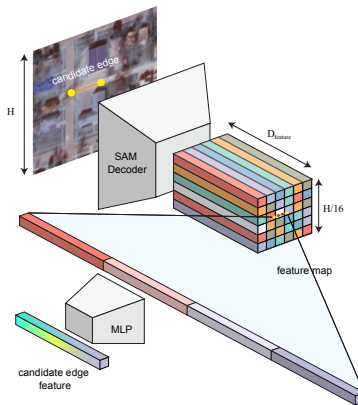
To evaluate the effectiveness of our proposed Coupled NMS, we compare it with the standard NMS used in prior work [18] for our proposed method with all other components fixed on both the City-scale and SpaceNet datasets. Results are summarized in Table 4.

We observe that Coupled NMS consistently improves the performance of our method, yielding higher recall, TOPO-F1, and APLS on both datasets.

**Table 4:** Performance comparison of NMS and Coupled NMS on the City-scale and SpaceNet datasets.

Methods	City-scale Dataset				SpaceNet Dataset			
	Prec.↑	Rec.↑	F1↑	APLS↑	Prec.↑	Rec.↑	F1↑	APLS↑
<b>Ours</b> w/ NMS	<b>91.62</b>	74.65	82.11	68.57	<b>93.47</b>	75.38	83.46	73.05
<b>Ours</b> w/ Coupled	91.09	<b>75.44</b>	<b>82.06</b>	<b>68.88</b>	92.82	<b>77.11</b>	<b>84.24</b>	<b>73.94</b>
<b>Ours</b> w/ Overpass w/ NMS	92.89	73.87	82.11	68.85	93.29	75.13	83.23	72.63
<b>Ours</b> w/ Overpass w/ Coupled	<b>92.75</b>	<b>76.64</b>	<b>83.77</b>	<b>70.40</b>	<b>93.50</b>	<b>76.38</b>	<b>84.08</b>	<b>73.36</b>

## B Candidate Edge Features from SAM Embedding

**Fig. 6:** Process of generating candidate edge features. Intermediate points are interpolated between edge endpoints, and features are sampled at these points using a bilinear sampler. The sampled features are then concatenated and passed through an MLP to produce the final edge feature.

As shown in Figure 6, We obtain the feature representation for each candidate edge by sampling visual features from the encoder feature map  $F$  using bilinear interpolation at both endpoints, as well as at a series of uniformly interpolated points along the edge. This sampling strategy captures contextual cues along the potential road segment. Specifically, we extract  $N_{sampled}$  feature vectors from positions evenly spaced between the two endpoints, concatenate them in order from the first to the second endpoint, and use the resulting sequence to represent the edge. The concatenated feature vector is then passed through a multilayer perceptron (MLP) to generate the final candidate edge embedding, which serves as input to the graph reasoning module for connectedness prediction.

## C Effect of Overpass/Underpass Segmentation Head

**Table 5:** Results for models with overpass head on the City-scale dataset.

Methods	City-scale Dataset			
	Prec.↑	Rec.↑	F1↑	APLS↑
SAM-Road [18]	<b>90.47</b>	67.69	77.23	<b>68.37</b>
SAM-Road [18] w/ Overpass	90.06	<b>68.16</b>	<b>77.40</b>	68.34
SAM-Road++ [44]	88.39	<b>73.39</b>	<b>80.01</b>	<b>68.34</b>
SAM-Road++ [44] w/ Overpass	<b>88.47</b>	72.54	79.48	67.34
<b>Ours</b>	91.09	75.44	82.37	68.88
<b>Ours w/ Overpass</b>	<b>92.75</b>	<b>76.64</b>	<b>83.77</b>	<b>70.40</b>

To evaluate the effectiveness of the proposed overpass/underpass segmentation head, we compare overpass version against the non-overpass version from prior work [18] across three models — SAM-Road, SAM-Road++, and LineGraph2Road — on the City-scale dataset (Table 6).

The overpass/underpass head consistently enhances our framework, yielding notable gains in precision recall, TOPO-F1, and APLS. In contrast, adding it to SAM-Road and SAM-Road++ offers limited or even negative effects. This contrast highlights that the head alone is insufficient without a model capable of reasoning over structured, global context, and might introduce variability. When integrated into LineGraph2Road, however, it complements the line-graph-based connectivity reasoning by explicitly modeling multi-level intersections, enabling the network to recover complex crossing structures that other model often miss.

## D Expressiveness of Model to Learn Structural Link Representation

We discuss the expressiveness of models for structural link representation learning. We first give the definition of the structural link representation.

**Definition 2. (Set-Isomorphism)** Given a graph  $G = (V_G, A_G)$ , two node subsets  $S, S' \subseteq V_G$  are said to be set-isomorphic, denoted  $S \simeq_G S'$ , if there is a permutation  $\pi \in \Pi_n$  such that  $\pi(A_G) = A_G$  and  $\pi(S) = S'$ .

**Definition 3. (Structural Representation)** For  $G = (V_G, A_G)$ ,  $S \subseteq V_G$  and let  $f(S, G)$  be a function that aims at learning a representation for the node set  $S$ . The function  $f(S, G)$  is said to be a most expressive structural representation, if for all  $S, S' \subseteq V_G$ ,  $f(S, G) = f(S', G) \iff S \simeq_G S'$ . When  $|S| = 2$ , we refer to it as the most expressive structural link representation, and when  $|S| = 1$ , we refer to it as the most expressive structural node representation.

We do not consider labeling trick methods [47], as they typically prevent the model from predicting all links in a single GNN inference step, leading to reduced efficiency.

### D.1 Graph Autoencoders Fails

For the discussion, we first give the definition of Node-most-expressive GNN [47].

**Definition 4. (*Node-most-expressive GNN*)** A GNN is node-most-expressive if for any graph  $G = (V_G, A_G)$ ,  $\forall i, j \in V_G$ ,  $GNN(i, A_G) = GNN(j, A_G) \Leftrightarrow i \simeq_G j$ .

As proved in [47], GAEs cannot learn a structural link representation, even when equipped with a *node-most-expressive GNN* that learns a structural node representation. This is demonstrated by presenting examples of multi-node representation learning problems involving more than two nodes, showing that directly aggregating node representations from a GNN does not yield a structural representation for node sets.

Here, we provide examples based on the road network graph to illustrate that this issue also arises in the original graph we construct for connectedness prediction with node-most-expressive GNN as shown in Figure 8.

**Assumption D1** If  $\{i\} \simeq_G \{j\}$ ,  $i, j \in V_G$ , the initial node feature embeddings for them input to the GAE are necessarily identical.

While this assumption does not strictly hold in practice, it is a reasonable approximation supported by empirical evidence. Specifically, bilinearly sampled features corresponding to isomorphic nodes consistently exhibit high cosine similarity, as demonstrated in Figure 7.

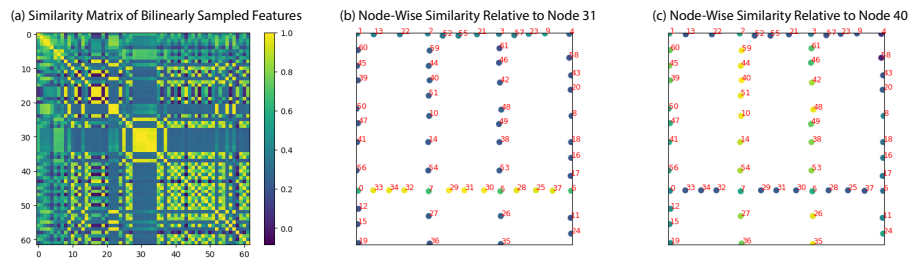


**Fig. 7:** Pairwise similarity of bilinearly sampled features across nodes in the graph. (a) The overall similarity matrix shows the pairwise feature similarities for all nodes. (b) Node-wise similarity relative to node 31. (c) Node-wise similarity relative to node 40.

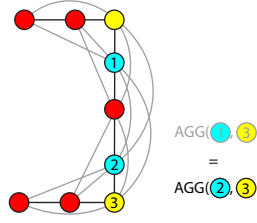


**Fig. 8:** directly aggregating node representations from a GNN does not yield a structural representation for node sets

In this example, we have  $\{1\} \simeq_G \{2\}$ , then by Definition 4, we will have  $\text{GNN}(\{1\}, A_G) = \text{GNN}(\{2\}, A_G)$ , and further we have

$$\text{AGG}(\text{GNN}(\{1\}, A_G), \text{GNN}(\{3\}, A_G)) = \text{AGG}(\text{GNN}(\{2\}, A_G), \text{GNN}(\{3\}, A_G)) \quad (6)$$

However,  $\{1, 3\}$  and  $\{2, 3\}$  is not *set-isomorphic*, so the aggregated most expressive structural node representation is not a most expressive structural link representation.

## D.2 Line Graph for Structural Link Representation

Now, we discuss the ability of Node-most-expressive GNN to learn structural link representation by line graph conversion.

**Theorem 1. (Whitney's Theorem)** *If two connected graphs have isomorphic line graphs, then the original graphs are isomorphic—except for the pair  $K_3$  and  $K_{1,3}$  [37].*

**Lemma 2.** *Given a connected graph  $G = (V_G, A_G)$  and its corresponding line graph  $L(G) = (V_{L(G)}, A_{L(G)})$ , we have  $i, j \in V_G, A_{ij} = 1$ , then  $ij \in V_{L(G)}$ . For link  $(i, j)$  in  $G$ ,  $f((i, j), G) = \text{GNN}(ij, A_{L(G)})$  is the most expressive structural link representation, if the GNN is node-most-expressive and  $G \notin \{K_3, K_{1,3}\}$ .*

*Proof.* According to Definition 3, as long as for all  $\{i, j\}, \{k, l\} \subseteq V_G$  and  $A_{ij} = A_{kl} = 1$ ,  $\text{GNN}(ij, A_{L(G)}) = \text{GNN}(kl, A_{L(G)}) \iff \{i, j\} \simeq_G \{k, l\}$ , then  $f((i, j), G) = \text{GNN}(ij, A_{L(G)})$  is the most expressive structural link representation.

$$\begin{aligned} \text{GNN}(ij, A_{L(G)}) &= \text{GNN}(kl, A_{L(G)}), \quad ij, kl \in V_{L(G)} \\ &\iff ij \simeq_{L(G)} kl \\ &\quad \text{(by Definition 4 and GNN is node-most-expressive)} \\ &\iff \exists \pi \in \Pi_m \text{ s.t. } \pi(A_{L(G)}) = A_{L(G)} \text{ and } \pi(ij) = kl \\ &\quad \text{(by Definition 2)} \\ &\iff \exists \pi' \in \Pi_n \text{ s.t. } \pi'(A_G) = A_G \text{ and } \pi'(\{i, j\}) = \{k, l\} \\ &\quad \text{(by Theorem 1 and graph } G \notin \{K_3, K_{1,3}\}) \\ &\iff \{i, j\} \simeq_G \{k, l\} \end{aligned}$$

This concludes the proof.

While triangles ( $K_3$ ) and 3-star graphs ( $K_{1,3}$ ) are theoretical exceptions to line-graph isomorphism, they almost never occur as isolated components in real road networks. Genuine instances—such as a standalone roundabout with no connecting roads or an isolated three-way split of very short segments—are exceedingly rare and largely artificial. To confirm this empirically, we scanned two large datasets with Algorithm 2.

---

**Algorithm 2** Counting Isolated  $K_3$  and  $K_{1,3}$  Components

---

```

1:  $count\_K_3 \leftarrow 0, count\_K_{13} \leftarrow 0$ 
2: for each  $id$  in  $ids$  do
3:    $G \leftarrow load\_graph(id)$ 
4:   for each  $comp$  in  $connected\_components(G)$  do
5:     if  $|comp| = 3$  and every node has degree 2 within  $comp$  then
6:        $count\_K_3 \leftarrow count\_K_3 + 1$ 
7:     else if  $|comp| = 4$  and one node has degree 3 and three nodes have degree 1
       within  $comp$  then
8:        $count\_K_{13} \leftarrow count\_K_{13} + 1$ 
9:     end if
10:  end for
11: end for

```

---

This yields: City-Scale (over 755 km<sup>2</sup>) contains 1 instance of  $K_3$  and 10 instances of  $K_{1,3}$ , while SpaceNet (over 407 km<sup>2</sup>) contains 0 instances of  $K_3$  and 9 of  $K_{1,3}$ . These counts confirm that truly isolated  $K_3$  and  $K_{1,3}$  patterns are negligible in practice, indicating that the theoretical exception has minimal impact on our method’s validity.

### D.3 Comparison with Standard GNN Baselines as Graph Autoencoders on the Line Graph

**Table 6:** Results for models with overpass head on the City-scale dataset.

GNN (w/ Overpass )	City-scale Dataset				
	Prec.↑	Rec.↑	F1↑	APLS↑	Time per Image (s)
GCN [22]	92.92	75.67	83.24	70.14	10.51
GAT [35]	92.97	75.85	83.34	70.22	10.74
SAGE [12]	93.59	72.44	81.37	64.13	10.64
GIN [40]	92.81	76.13	83.49	<b>70.54</b>	10.48
<b>Ours (Graph Tranformer [30])</b>	92.75	76.64	<b>83.77</b>	70.40	10.51

Inference time for  $5 \times 5$  sliding windows

Table 6 reports the performance of different GNN-based graph autoencoders (GCN, GAT, GraphSAGE, and GIN) using the same line-graph representation and training protocol with an overpass prediction head on the City-scale dataset. The comparison shows that while the line-graph representation itself provides a strong foundation, our Graph Transformer consistently achieves the best overall F1 score and recall, while maintaining comparable computational cost to the simpler GNN variants. We adopt the Graph Transformer architecture [30] to preserve a transformer-based design consistent with [18, 44], ensuring that the observed performance gains stem from enhanced graph reasoning rather than differences in model class.

## E Pipeline for Preprocessing Training Data

Algorithm 3 outlines the iterative graph refinement process used to disentangle stacked road intersections and identify potential overpass/underpass crossing structures. Starting from an initial road graph  $G_0$ , the algorithm repeatedly adjusts node positions based on local geometric conflicts detected through edge intersections. For each intersecting pair of edges, nodes within a proximity threshold  $\tau$  are shifted along their incident directions to reduce overlap. Every  $P$  iterations, degree-2 nodes forming near-parallel, closely spaced connections ( $\text{gap} < \gamma$ ) are merged to collapse redundant stacked segments. The iterative relocation continues until all node displacements fall below the tolerance  $\varepsilon$ , yielding a refined graph  $G$  in which true overpasses/underpasses crossing remain geometrically separated while false planar intersections are resolved.

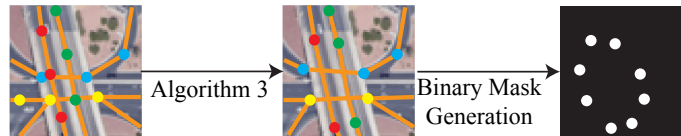


**Fig. 9:** Overpass/underpass masks generation process

To finally generate the overpass/underpass masks, we focus on the endpoints of edges identified as geometrically separated yet intersecting overpass/underpass crossings by Algorithm 3, and convert them into binary masks that serve as supervision targets for our model.

Figure 10 illustrates a process for generating candidate edges with label for training data. Initially, only the keypoints are retained, and additional nodes are randomly interpolated between them with intervals sampled from a uniform distribution  $U(d_r, 2d_r)$  according to Algorithm 4. Coupled NMS is then applied to both the keypoints and interpolated nodes to refine the set of vertices. Algorithm 3 is used to detect the endpoints of edges involved in overpass/underpass crossings and adjust them to suitable locations. Vertex pairs within a specified

---

**Algorithm 3** Iterative Graph Refinement for Road Network Overpass/Underpass Detection and Adjustment

---

```

1: //  $\tau$ : intersection threshold,  $\gamma$ : merge gap,  $\alpha$ : step scale
2: //  $T$ : max iterations,  $P$ : merge period,  $\varepsilon$ : tolerance
3:  $G \leftarrow G_0$ 
4: for  $t = 1$  to  $T$  do
5:   Build spatial index over edges;  $\Delta \leftarrow \emptyset$ 
6:   for each intersecting edge pair  $(a, b), (c, d)$  without shared endpoints do
7:     for each endpoint  $v \in \{a, b, c, d\}$  do
8:        $d \leftarrow \|v - p\|$ 
9:       if  $d < \tau$  then
10:         $\hat{u} \leftarrow$  unit vector from  $v$  to its neighbor
11:         $\Delta[v] += ((\tau - d)/\tau) \cdot \hat{u}$ 
12:       end if
13:     end for
14:   end for
15:   if  $t \bmod P = 0$  then
16:     // Contract stacked nodes
17:     for each node  $k$  with  $\deg(k) = 2$  and  $\text{gap}(k) < \gamma$  do
18:       Connect its two neighbors and remove  $k$ 
19:     end for
20:   else
21:      $moved \leftarrow 0$ 
22:     for each node  $v$  with adjustment  $\mathbf{a} = \Delta[v]$  do
23:       if  $\|\mathbf{a}\| > \varepsilon$  then
24:          $\hat{\mathbf{a}} \leftarrow \mathbf{a}/\|\mathbf{a}\|$ 
25:          $v' \leftarrow v + \alpha\hat{\mathbf{a}}$ 
26:         if  $v'$  not overlapping other nodes then
27:           Move  $v$  to  $v'$ ,  $moved \leftarrow moved + 1$ 
28:         end if
29:       end if
30:     end for
31:     if  $moved = 0$  then
32:       break // converged
33:     end if
34:   end if
35: end for
36: return  $G$ 

```

---

distance threshold  $d_{nei}$  are connected, forming potential edges. These pairs are considered as candidate edges, which are subsequently labeled based on the connection criteria.

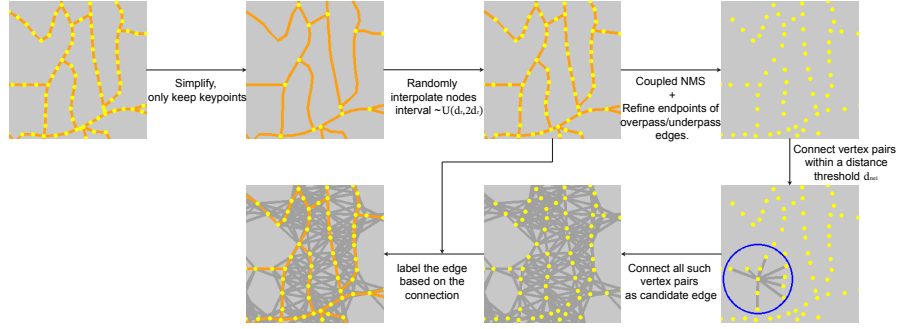


**Fig. 10:** Pipeline for preprocessing the original road network graph into the final graph used for classification.

---

#### Algorithm 4 Randomly Interpolate Nodes Along a Line

---

```

1: //  $d_r$ : road suppression radius
2:  $D \leftarrow \emptyset$  //List of sampled distances
3:  $p \leftarrow 0$  //Current position
4:  $L \leftarrow$  length of the line
5: while  $p + 2 \cdot d_r - 1 < L$  do
6:   Sample  $u \sim \mathcal{U}(d_r, 2 \cdot d_r - 1)$ 
7:   if  $p + u + d_r - 1 < L$  then
8:      $p \leftarrow p + u$ 
9:     Append  $p$  to  $D$ 
10:  end if
11: end while
12: return  $D$ 

```

---

## F Additional Visual Comparison

### F.1 More Qualitative Comparison on City-scale Dataset

We provide additional visualizations in Figure 11 to further demonstrate our model’s ability to capture complex topological structures. Figure 11c,d,e show our model’s promising performance for overpass scenarios. In Figure 11c, two

parallel lateral highways pass over three vertical roads, and the model correctly avoids predicting false intersections between the lower lateral highway and the vertical roads. A similar result is observed in Figure 11d, where the curved highway is appropriately separated from the vertical highway. Nonetheless, some limitations remain: in Figure 11c, the upper lateral highway is fragmented; in Figure 11d, the rightmost vertical lines are partially broken. In Figure 11e, the curved highway is incorrectly connected to nearby lanes. Despite these imperfections, our model captures the overall geometry more accurately than existing methods, which often fail to preserve the curved structure altogether.

Additional visualizations in Figure 12 further highlight our overpass variant’s capability to accurately capture complex overpass and underpass crossings.

## F.2 Failure Cases of Global-Scale Dataset

We present representative failure cases from the Global-scale dataset in Figure 13, which we categorize into three types. The first involves occlusions caused by tunnels, dense vegetation, or tall buildings, as shown in Figure 13a. The second type stems from incorrect or missing labels in the test set as shown in Figure 13b, which is an inevitable issue in large-scale datasets and can lead to an underestimation of model performance. The third category includes small unpaved roads or informal paths as shown in Figure 13c. This case highlights a broader challenge of domain shift and annotation inconsistency in large-scale, globally sourced datasets. Specifically, the failure involves small unpaved or informal roads, which are difficult to detect for several reasons. First, the dataset combines imagery from diverse geographic and socioeconomic regions. In rural or remote areas, unpaved roads and informal paths are often annotated as valid roads. However, in urban areas or even other rural areas, similar features are either unlabeled or inconsistently labeled. For example, the upper part of 5th row of Figure 13c has two unpaved small roads without labels according to the ground truth. This lack of consistent ground truth introduces ambiguity during training, where visually similar features may be considered "road" in one area and "non-road" in another. Second, small and unpaved roads often have limited contrast with the surrounding environment, especially in agricultural or arid regions, making it difficult for the model to detect them without clear boundaries. The model struggles to distinguish these paths from the background without sufficient training data. Third, our current model is trained on the full dataset without explicit domain adaptation techniques. As a result, it lacks the ability to adapt to regional visual and labeling differences.

## F.3 Connectivity Recovery under Occlusions

Graph reasoning enables the recovery of connectivity across occluded segments by propagating messages from nearby unoccluded nodes. We illustrate this capability with examples of tree-occluded roads in Fig. 14 for both City-Scale and Global-Scale dataset.

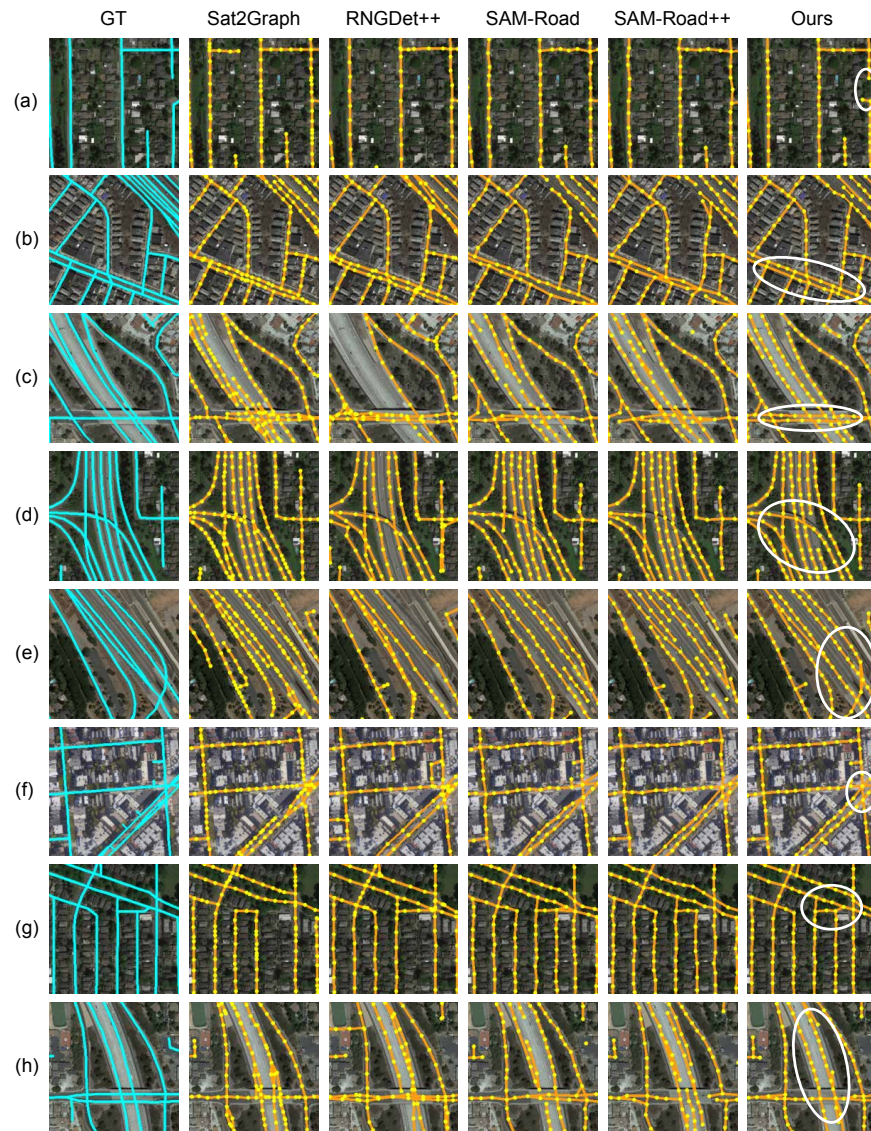


**Fig. 11:** Additional visualizations showing the model’s ability to capture complex topologies, including overpasses (panels c–e). While some imperfections remain, the model often avoids false intersections and preserves overall road geometry better than existing methods.

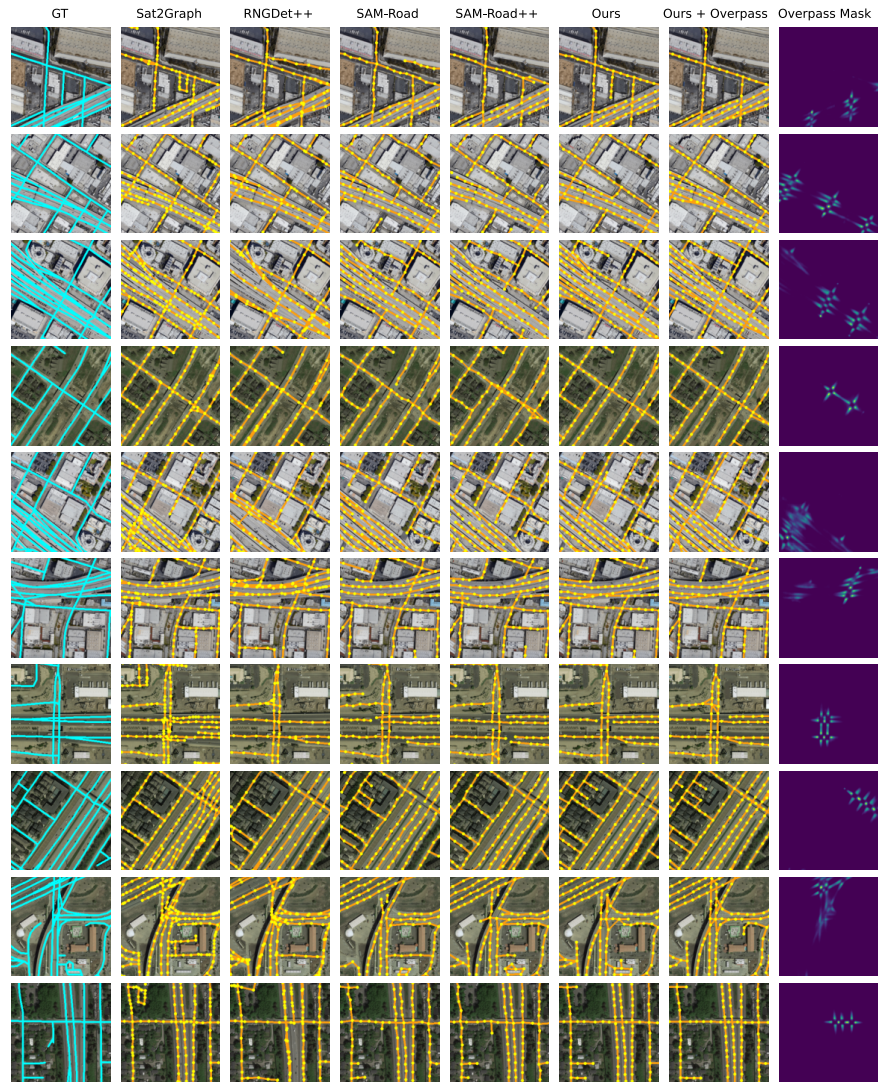


**Fig. 12:** Additional visualized road network graph predictions of our method and other baseline methods as well as the predicted overpass/underpass mask on City-Scale dataset, illustrating performance on overpass and underpass intersections.

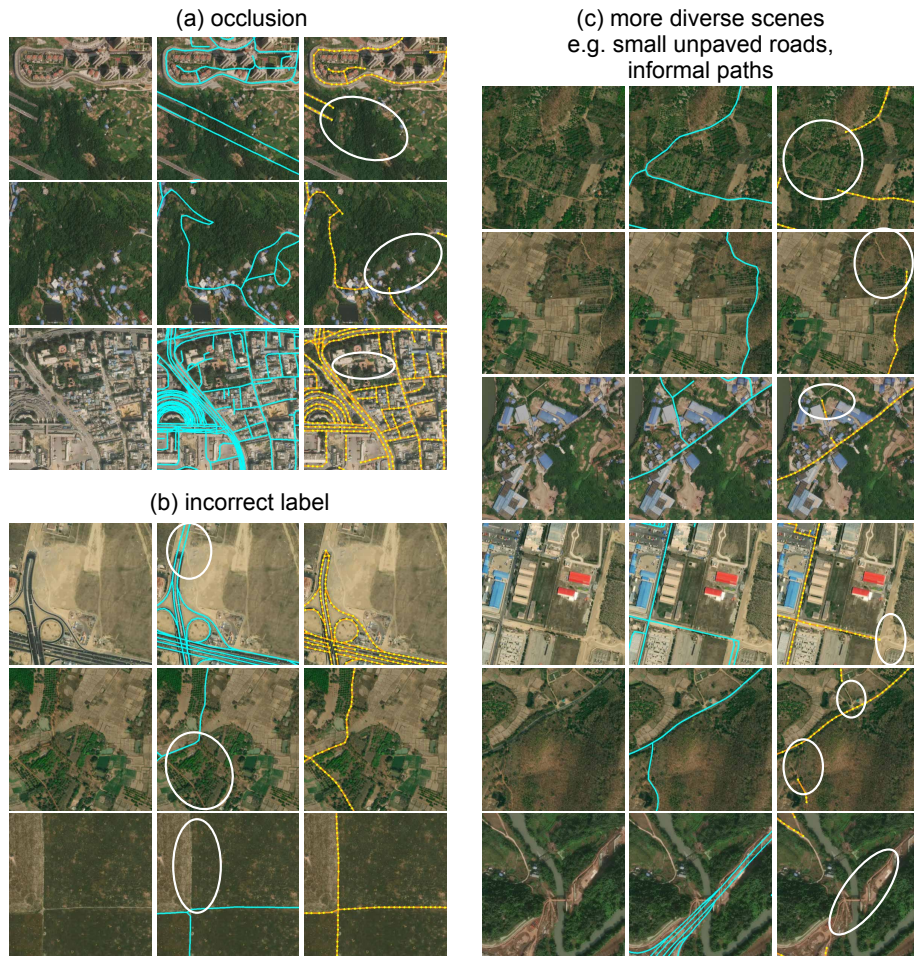


**Fig. 13:** Representative failure cases on the Global-scale dataset. (a) Missed roads due to occlusions from tunnels, vegetation, or tall buildings. (b) Incorrect or missing labels in the test set. (c) Missed detections of small unpaved or informal roads, reflecting domain shifts across diverse geographic regions.

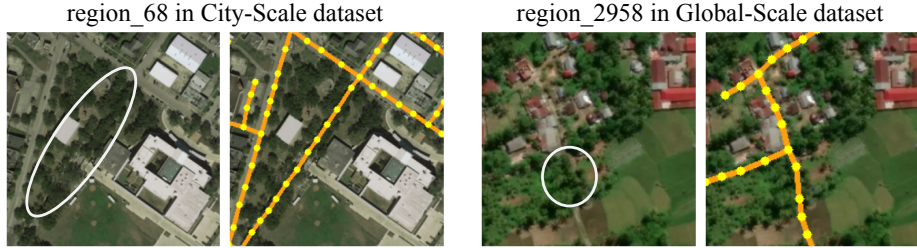


**Fig. 14:** Examples where our method successfully recovers connectivity for tree-obscured roads.

## G Sliding Window

During inference, we use a  $16 \times 16$  sliding window for the City-scale and Global-scale datasets, while the SpaceNet dataset is processed without windowing. To assess the impact of window sparsity, we evaluate performance using a reduced  $5 \times 5$  sliding window configuration on  $2048 \times 2048$  images, where each window has a size of  $512 \times 512$ . The  $5 \times 5$  setting is the smallest number of sliding windows that fully covers the image with an overlap greater than the neighborhood threshold  $d_{nei} = 64$ . As shown in Table 7, reducing the number of windows has minimal impact on overall performance. In fact, the APLS score slightly improves under the  $5 \times 5$  configuration for the non-overpass variant on the City-scale dataset and the overpass variant on the Global-scale dataset. In all cases, both metrics under the  $5 \times 5$  setting still exceed those of all baseline methods.

**Table 7:** Comparison with  $5 \times 5$  and  $16 \times 16$  sliding windows on City-scale and Global-scale datasets.

Methods	City-scale Dataset				Global-scale(In-Domain)			
	Prec.↑	Rec.↑	F1↑	APLS↑	Prec.↑	Rec.↑	F1↑	APLS↑
SAM-Road [18]	90.47	67.69	77.23	68.37	91.93	45.64	59.80	59.08
SAM-Road++ [44]	88.39	73.39	80.01	68.34	88.95	49.27	62.33	62.19
<b>Ours</b> $5 \times 5$	90.28	75.93	82.35	69.05	90.07	50.81	64.03	66.58
<b>Ours</b> $16 \times 16$	91.09	75.44	82.37	68.88	90.54	51.12	64.43	67.69
<b>Ours w/ overpass</b> $5 \times 5$	92.54	75.60	83.01	70.58	87.31	53.06	65.26	69.66
<b>Ours w/ overpass</b> $16 \times 16$	92.75	76.64	83.77	70.40	89.65	50.85	64.05	68.70

## H Inference Time

We evaluate the inference efficiency of our model on the SpaceNet, City-scale, and Global-scale datasets using a single NVIDIA A100 GPU. As summarized

in Table 8, inference on small image tiles, such as those in SpaceNet, is computationally efficient. In contrast, the City-scale and Global-scale datasets involve larger input image size, requiring the use of sliding windows and thereby incurring higher computational costs. However, when employing a reduced  $5 \times 5$  sliding window configuration—which, as shown in Section G, maintains comparable performance—inference time is significantly reduced. This demonstrates the practicality of our approach for large-scale applications without compromising accuracy.

**Table 8:** Inference times for our model on three datasets using a single NVIDIA A100 GPU

Dataset	Image Size	# Test Images	Sliding Windows	Total Time (s)	Time per Image (s)
SpaceNet	400	382	No	115.87	0.30
City-scale	2048	27	$16 \times 16$	2354.27	87.19
			$5 \times 5$	283.97	10.51
Global-scale	2048	624	$16 \times 16$	47527.00	67.16
			$5 \times 5$	5012.74	8.03

We further compare the inference time of our model with SAM-Road [18] and SAM-Road++ [44] using a single NVIDIA A100 GPU. These two methods have been shown to be significantly more efficient than earlier approaches such as Sat2Graph [15] and RNGDet++ [42], with SAM-Road achieving up to  $80\times$  speedup. In our comparison, we use the  $5 \times 5$  sliding window configuration for our model, while reporting the results of SAM-Road and SAM-Road++ under their standard  $16 \times 16$  sliding window setting. This is because their performance degrades with fewer windows; for example, the APLS score of SAM-Road on the City-scale dataset drops from 68.37 to 67.21 when reducing the window configuration from  $16 \times 16$  to  $8 \times 8$ . With  $5 \times 5$  sliding window, our method achieves faster inference on both the City-scale and SpaceNet datasets as shown in Table 9, at the same time, have better performance.

**Table 9:** Total inference time comparison on City-scale and SpaceNet dataset

Method	City-scale Dataset	SpaceNet Dataset
SAM-Road	551.19 s	918.47 s
SAM-Road++	576.51 s	752.25 s
Our	283.97 s	115.87 s

## I Effect of Joint Training with LineGraph2Road on SAM Segmentation Performance

To assess whether the relation reasoning module in LineGraph2Road can guide the training of segmentation features, we compare the performance of the SAM when trained independently versus when jointly trained within the LineGraph2Road framework. We evaluate both approaches on road and keypoint segmentation tasks using the City-scale and SpaceNet dataset. We use mIOU to evaluate the performance, which is defined by the overlap between the predicted segmentation and the ground truth, divided by the total area covered by the union of the two. As shown in Table 10, integrating SAM into the end-to-end training pipeline of LineGraph2Road yields a slight improvement in segmentation performance.

**Table 10:** Comparison of segmentation performance (mIoU) on the City-scale and SpaceNet dataset.

Methods	City-scale Dataset		SpaceNet Dataset	
	Road	Keypoint	Road	Keypoint
SAM (independent training)	42.17	26.35	46.07	28.38
SAM (with LineGraph2Road)	<b>42.54</b>	<b>27.37</b>	<b>46.27</b>	<b>28.51</b>

While segmentation quality remains stable, joint training provides a clear advantage in graph-level reasoning—an essential capability for downstream topological tasks. In contrast, a SAM encoder-decoder trained in isolation cannot produce meaningful feature for graph structure inference.

To further examine this effect, we conduct an ablation study comparing joint and sequential training strategies. In the sequential setup, the SAM encoder-decoder is first trained for segmentation and then frozen, while the graph transformer on the line graph is trained separately. As reported in Table 11, this decoupled approach significantly reduces performance on the City-scale dataset.

**Table 11:** Effect of joint versus separate training on the City-scale dataset.

Model	Prec.↑	Rec.↑	F1↑	APLS↑
Train separately	92.18	56.82	69.82	46.42
Train jointly	<b>91.09</b>	<b>75.44</b>	<b>82.37</b>	<b>68.88</b>

These results demonstrate that joint training enables the encoder to adapt its features for more effective topology extraction, achieving substantial improvements in graph accuracy without compromising segmentation mIoU.